

# AKARI and Spinning Dust Emission

## A look at microwave dust emission via the Infrared

A. Bell, T. Onaka, F. Galliano, R. Wu, M. Hammonds, Y. Doi, D. Ishihara, M. Giard

*University of Tokyo, Bunkyo, Tokyo, Japan, 113-0033;*

*abell@astron.s.u-tokyo.ac.jp*

### ABSTRACT

*Subject headings:* AME, spinning dust, PAH bands, AKARI

#### 1. Introduction

Since its first detection in early microwave surveys, the anomalous microwave emission/foreground (AME) has been found to be a widespread feature of the microwave Milky Way (Dickinson et al. 2013). Kogut et al. (1996); de Oliveira-Costa et al. (1997); Leitch (1998) showed that the AME correlates very well with infrared emission from dust, via COBE/DIRBE and IRAS far-IR maps. However there is still much mystery, except that the most likely source of the AME is interstellar dust (Ysard & Verstraete 2010; Tibbs et al. 2011; Hensley et al. 2016).

From the observed spatial correlation between AME and dust emerged two prevailing hypotheses:

1) Electric dipole emission by spinning small dust grains, a mechanism proposed in Erickson (1957) and Hoyle & Wickramasinghe (1970), with further discussion in Ferrara & Dettmar (1994). Draine & Lazarian (1998) give the earliest thorough description, with substantial updates contributed more recently by Ysard & Verstraete (2010), Ali-Haïmoud et al. (2009), Hoang et al. (2010) and several others. Dickinson et al. (2013) provide a detailed overview of AME and spinning dust literature.

2) Magnetic dipole emission, caused by thermal fluctuations in grains with magnetic inclusions, proposed by Draine & Lazarian (1999).

More recently, modeled spectra for potential candidate carriers have appeared in the literature: PAHs, grains with magnetic inclusions (Draine

& Hensley 2013; Ali-Haïmoud 2014; Hoang et al. 2016).

A third, but not widely accepted, possible explanation for AME is discussed in Jones (2009). They have suggested that the emissivity of dust, in the spectral range related to AME, could contain features caused by low temperature solid-state structural transitions.

Although spinning dust need not be the only emission mechanism, the photometric signature of the AME, has so far been commonly explained via spinning dust parameters (Ysard et al. 2011; Ali-Haïmoud 2010). In this paper, we explore the case that the AME signature arises from spinning dust emission. If the AME is carried by spinning dust, the most likely candidate that has been proposed so far is the polycyclic aromatic hydrocarbon family of molecules (PAHs). PAHs are hydrocarbons based on fused carbon rings. Those PAHs which have a permanent electric dipole (i.e. coronulene, but not symmetric molecules like coronene), can emit rotationally.

The mid-infrared “PAH features” are ubiquitous in the ISM (Giard et al. 1994; Onaka et al. 1996; Onaka 2000), such that the carriers must be abundant. There has not yet been a conclusive identification of any particular PAH species. However Andrews et al. (2015) strongly argue for the existence of a dominant “grandPAH” class, containing 20 to 30 PAH species.

Assuming a rotational emission model, the AME signature (consistent with continuum emis-

sion having a peak around 20 to 40 GHz ) implies very small oscillators ( $\sim 10$  nm). In any case, the PAH class of molecules are the only spinning dust candidate so far which show both: 1) Evidence of abundance in the ISM at IR wavelengths, and 2) A predicted range of dipole moments (on order of 1 debye), to produce the observed AME signature (Draine & Lazarian 1998; Lovas et al. 2005; Thorwirth et al. 2007). However, it should be noted that the current upper-bound on the abundance of nanosilicates, allows for a "spinning nanosilicate" explanation for the AME, as shown by Hensley & Draine (2017). Due to the (apparently) continuous shape of the AME SED, a distribution of dipole moments and rotational velocities is needed, in a spinning dust scenario.

The overall pattern among large-scale studies seems to show that all of the dust-tracing photometric bands show evidence of at least a first-order correlation with the AME (and each other.) On an all-sky, pixel-by-pixel basis, at 1-degree angular resolution, Ysard et al. (2010) find that  $12\ \mu\text{m}$  emission, via IRAS, correlates more strongly with AME (via WMAP) than with  $100\ \mu\text{m}$  emission. They also find that scaling the IR intensity by the interstellar radiation field strength (given as  $G_0$ , a measure of ISRF relative to that of the solar neighborhood) improves both correlations.

However in a similar work, Hensley et al. (2016) report that the  $12\ \mu\text{m}$  emission (via WISE) correlates less tightly with AME than with thermal dust radiance, using the Planck Collaboration dust and AME component-separation maps (Planck Collaboration et al. 2016a). Also at odds with Ysard et al. (2010), they report that AME correlates more strongly with  $12\ \mu\text{m}$  intensity than with the intensity scaled by the interstellar radiation field.

The story is no more clear when looking at the average properties of individual regions. Planck Collaboration et al. (2014c) find that among 22 high-confidence "AME regions" (galactic clouds such as the  $\rho$  Ophiuchus cloud and the Perseus molecular cloud complex) AME vs.  $12\ \mu\text{m}$  shows a marginally weaker correlation than AME vs.  $100\ \mu\text{m}$  (via IRAS).

In this work, we attempt to reach some stronger consensus on the large-scale AME vs. IR-dust story. In Section 2, we describe the all-sky surveys and component maps used in this paper. The

sources range from PAH-dominated MIR bands from AKARI and IRAS to FIR and microwave-derived maps from Planck Observatory. These bands are listed in table 2, and are outlined in the following Data section. Section 3 describes our investigation approach: looking at all-sky trends, a circular aperture photometry on a list of regions of interest, and a localized study of the AME region of largest angular size, lambda Orionis. Section ?? describes the conclusions of these 3 approaches, and compares them to previous AME vs. dust emission studies.

We utilize the newly created AKARI/IRC  $9\ \mu\text{m}$  all-sky map, which more completely covers PAH features than previous all-sky surveys, and has the highest fractional contribution from PAH emission, as can be seen in Fig. 2.1, assuming a PAH and grain SED model such as Draine & Li (2001). This is especially true as the interstellar radiation field (ISRF) intensifies, and the IRAS or WISE  $12\ \mu\text{m}$  bands include more continuum emission.

## 2. Data

This work relies completely on all-sky surveys. All of the maps utilized are photometric-band infrared maps, except for the AME data, which is an all-sky component separation analysis product, from the Planck Collaboration's efforts to separate galactic foregrounds from the CMB.

We are primarily interested in the AKARI/IRC  $9\ \mu\text{m}$  band's unique coverage of the PAH bands at  $6.2$ ,  $7.7$ ,  $8.6$ , and  $11.2\ \mu\text{m}$ , and if this shows any stronger/weaker correlation with AME than the WISE or IRAS  $12\ \mu\text{m}$  bands. In total, we use all-sky maps from 19 photometric bands, spanning the wavelength range of  $6.9\ \mu\text{m}$  to  $550\ \mu\text{m}^{***}$

### 2.1. Infrared Data

The AKARI infrared space telescope revealed an entire sky of infrared light, from the mid to far infrared, via two instruments (Murakami et al. 2007) the Infrared Camera (IRC)(Onaka et al. 2007) and the Far Infrared Surveyor (FIS) (Kawada et al. 2007a).

IRC's  $9\ \mu\text{m}$  band all-sky map demonstrates the abundance of the PAH bands carrier in the Milky Way (Ishihara et al. 2010). Figure 2.1 shows the coverage of the MIR bands along with an example

galactic cirrus SED. The  $9\text{ }\mu\text{m}$  band uniquely covers major ionized PAH features at  $6.2$  and  $7.7\text{ }\mu\text{m}$ ; as well as neutral PAH features at  $8.6$  and  $11.2\text{ }\mu\text{m}$  across the entire sky (Onaka et al. 2007). The IRAS  $12\text{ }\mu\text{m}$  band covers the  $11.2$  and  $8.6\text{ }\mu\text{m}$  features, and the similarly-shaped WISE  $12\text{ }\mu\text{m}$  band covers primarily the  $11.2\text{ }\mu\text{m}$  feature. According to this distribution of PAH features across the response filters, it is expected that the IRC  $9\text{ }\mu\text{m}$  band is the one most dominated by PAH emission. Figure 2.1 shows the relative contribution of neutral PAHs vs ionized PAHs to the AKARI/IRC  $9\text{ }\mu\text{m}$ , IRAS  $12\text{ }\mu\text{m}$  and WISE  $12\text{ }\mu\text{m}$  bands, based on the DL01 dust SED model. IRC  $9\text{ }\mu\text{m}$  shows a larger contribution from ionized PAHs, by about 16 percent, and a conversely smaller contribution from neutral PAHs. These relative contributions remain relatively constant out to a  $G_0$  of about 100, with the contribution from warm dust becoming a larger factor for the IRAS  $12\text{ }\mu\text{m}$  and WISE  $12\text{ }\mu\text{m}$  bands. Thus, according to the DL01 template, IRC  $9\text{ }\mu\text{m}$  should have the highest contribution from PAHs (especially ionized) out to extreme radiation fields.

We utilize the most recent version of the IRC data (Ishihara, et al., in prep.) This version has had an updated model of the Zodiacaal light, fitted and subtracted. The details of the improved Zodi-model, which offers an improvement over that used for the IRAS all-sky maps, are given in Kondo et al. (2016).

The AKARI Far Infrared Surveyor (FIS) gives us photometric data around the peak of the typical thermal dust SED. FIS was equipped with four wavebands: two narrow bands centered at  $65\text{ }\mu\text{m}$  and at  $160\text{ }\mu\text{m}$ , and two wide bands at  $90\text{ }\mu\text{m}$  and at  $140\text{ }\mu\text{m}$ . An all-sky survey was carried out at each band (Kawada et al. 2007b), and the processed maps have been publicly released (Doi et al. 2015).

The Planck Space Observatory (Planck) High Frequency Instrument (HFI) all-sky maps, spanning 100 to 857 GHz (Planck Collaboration et al. 2014a) constrain the far IR dust emissivity. This study utilizes the 857 GHz ( $345\text{ }\mu\text{m}$ ) and 545 GHz ( $550\text{ }\mu\text{m}$ ) bands.

Data from the Infrared Astronomical Satellite (Neugebauer et al. 1984) all-sky surveys are used to supplement the similarly-centered AKARI photometric bands. The IRAS  $12\text{ }\mu\text{m}$  band is sim-

ilar to the AKARI  $9\text{ }\mu\text{m}$  band in terms of the sky coverage, central wavelength, and especially in that both surveys are heavily dominated by zodiacal light. We use the Improved Reprocessing of the IRAS Surveys (IRIS) (Miville-Deschénes & Lagache 2005), which use undergone a zodiacal-light removal. The Zodiacaal light model, however differs between the two bands. The IRAS Zodi-subtraction is primarily based on the Kelsall et al. (1998) model.

## 2.2. AME Data

We utilize the AME component separation map, from the Planck Collaboration's Public Data Release 2. Details of the foreground contribution estimates are given in Planck Collaboration et al. (2014b). We caution readers that this AME map was created primarily for the purpose of isolating the CMB from galactic microwave emission. It is not to be taken as a perfect isolation of the AME. We employ it in this work, simply because there is no other all-sky AME estimate available. We also quote AME estimates for 98 circular apertures, found in Planck Collaboration et al. (2014c), that were made using a more careful region-by-region component separation method at 1-degree resolution.

## 2.3. All-sky Data Processing

The HFI, FIS, and IRIS maps used here are downloaded from their respective online repositories, as all-sky HEALPix (Górski et al. 2005) NSIDE 2048 maps. In the case of the IRC maps, we first create HEALPix maps from the 4,857 all-sky survey tiles using the Aladin all-sky data visualization platform (Bonnarel et al. 2000). NSIDE 2048 implies an average pixel spacing of  $1.7'$ . The maps are then degraded to NSIDE 1024 before carrying out the Gaussian-beam smoothing to a 1-degree FWHM. Following the smoothing process, the maps are degraded once more to NSIDE 256. The value of each of the larger NSIDE 256 pixels, comes from the mean of its parent NSIDE 1024 pixels. The purpose of this processing is to ensure that all of the maps have the same resolution as the PR2 AME map.

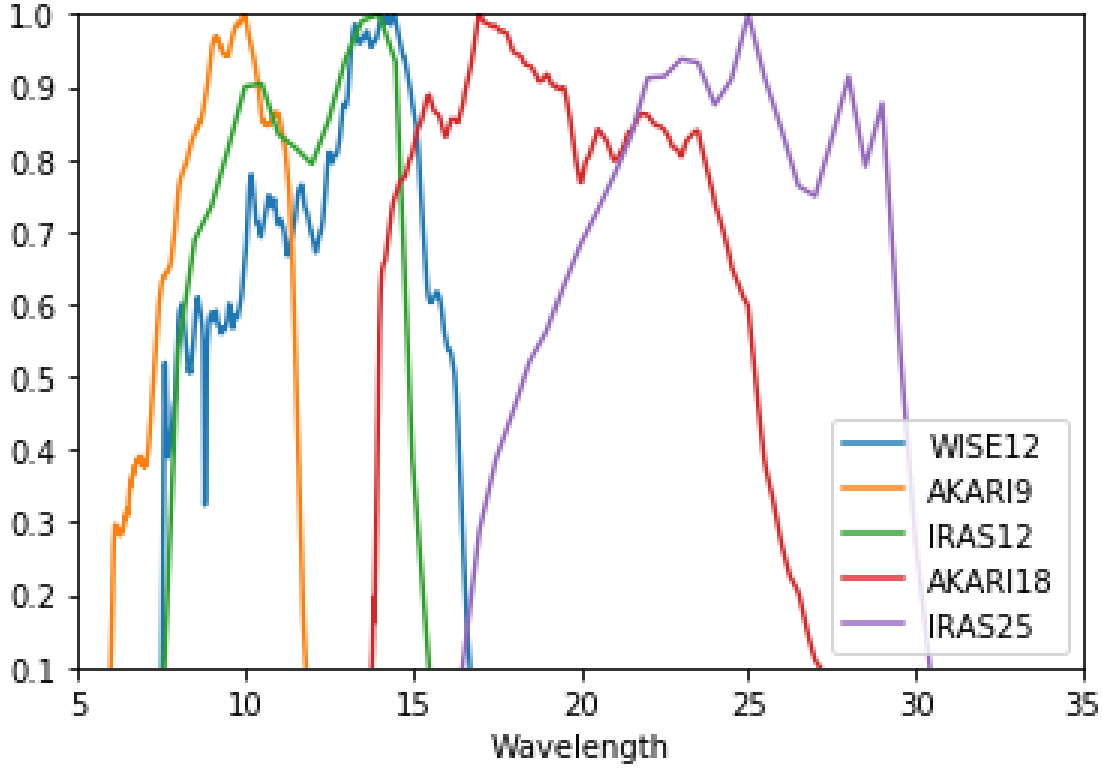


Fig. 1.— Relative spectral response curves of the MIR bands used in this study, AKARI/IRC 9  $\mu\text{m}$ , IRAS 12  $\mu\text{m}$ , WISE 12  $\mu\text{m}$ , AKARI 18  $\mu\text{m}$ , and IRAS 25  $\mu\text{m}$ . AKARI/IRC 9  $\mu\text{m}$ , IRAS 12  $\mu\text{m}$ , WISE 12  $\mu\text{m}$  bands are dominated by PAH emission (see Figure 2.1. The AKARI 18  $\mu\text{m}$ , and IRAS 25  $\mu\text{m}$  bands contain minimal PAH emission.

Table 1: Observational data sources used in this article

Instrument	Central Wavelength	FWHM	Uncertainty	Reference
AKARI/IRC	9 $\mu\text{m}$	~10"	<10%	(Ishihara et al. 2010)
AKARI/IRC	18 $\mu\text{m}$	~10"	<10%	"
AKARI/FIS	65 $\mu\text{m}$	63"	<10%	(Doi et al. 2015; Takita et al. 2015)
AKARI/FIS	90 $\mu\text{m}$	78"	<10%	"
AKARI/FIS	140 $\mu\text{m}$	88"	<10%	"
AKARI/FIS	160 $\mu\text{m}$	88"	<10%	"
COBE/DIRBE	12 $\mu\text{m}$			
COBE/DIRBE	25 $\mu\text{m}$			
COBE/DIRBE	60 $\mu\text{m}$			
COBE/DIRBE	100 $\mu\text{m}$			
IRAS/IRIS	12 $\mu\text{m}$	4.0'	<5.1%	(Miville-Deschénes & Lagache 2005)
IRAS/IRIS	25 $\mu\text{m}$	4.0'	<15.1%	"
IRAS/IRIS	60 $\mu\text{m}$	4.2'	<10.4%	"
IRAS/IRIS	100 $\mu\text{m}$	4.5'	<13.5%	"
Planck/HFI	345 $\mu\text{m}$	4.7'		(Planck Collaboration et al. 2014a)
Planck/HFI	550 $\mu\text{m}$	4.3'		"
WISE	12 $\mu\text{m}$			

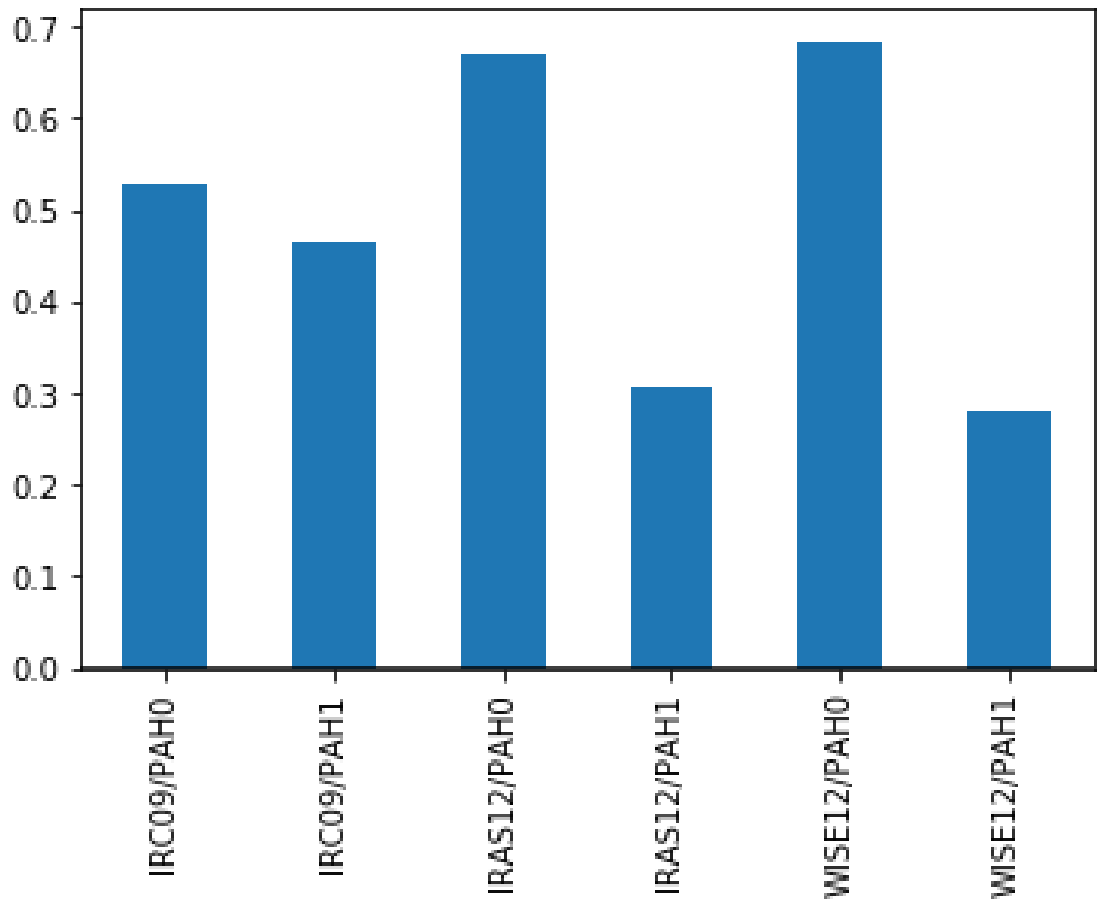


Fig. 2.— Fractional contribution of ionized vs. neutral PAH emission, based on the DL01 dust SED model at  $G_0$  of 1.  $G_0$  is the interstellar radiation field strength relative to that of the solar neighborhood. PAH0 and PAH1 refer to neutral and ionized PAHs.

### 3. Analysis

The analysis we have done so far is done from 3 perspectives, but with all 3 relying on 1-degree resolution, Planck-based AME data. We start from a widely-cast net: an AME to IR comparison on an all-sky basis, looking at trends among, essentially, all pixels in the all-sky maps except for those within 10 degrees of the ecliptic plane. Then we move to a slightly more regionalized comparison, looking at the set of AME-prominent galactic clouds identified by the Planck Collaboration et al. (2014c) (wherein we keep our analysis parallel to theirs, to maintain comparability between their IRAS-Planck based result, and our result which adds-in AKARI data and dust SED fitting.) Lastly, we highlight a particular AME-dominated region, the “Meissa ring”, otherwise known as the  $\lambda$  Orionis molecular ring (Maddalena 1986; Maddalena & Morris 1987). Our motivation is to highlight the limitations of low resolution AME data, at 3 different scales, and help to promote higher resolution, more localized, structural studies of AME and spinning dust.

#### 3.1. All-sky Pixel Domain Analysis

In order to look more closely at the variations between the individual bands’ maps, we also include a pixel-by-pixel analysis. Figure 3.1 shows the result of such a comparison, for each of the 19 bands sampled. The AME data comes from the AME component map provided in the Planck Public Release 2, produced by the COMMANDER component separation method.

To keep our analysis comparable to previous works, we carry-out the analysis by excluding pixels within 10 degrees of the ecliptic plane, where the Zodi-residuals can be a problem (especially in the MIR.) The remaining pixels are divided into “high galactic latitudes” (more than 10 degrees from the galactic plane), and “low to mid galactic latitudes” (within 10 degrees of the plane).

We can quickly see that, for all of the bands, there is a first-order correlation between the IR with the AME. Figure 3.1 visualizes the cross-correlation matrix for each of the IR bands and the AME for both the Pearson-based and Spearman-based cross-correlation matrices. With either test, the AME does not show a strong correlation with other bands at high latitudes. At lower latitudes,

the FIR bands show stronger correlation for the Pearson test, but there appears to be an even correlation across all bands in the case of the Spearman rank test. The AKARI 9 micron bands, and the other PAH-tracing bands show a stronger correlation only relative to the bands from 18 to 60 microns. The WISE 12 micron band is shown for comparison purposes, but the version of the WISE 12 micron map used here has been produced only for visualization purposes and is not yet vetted for scientific analysis.

Even excluding pixels near the ecliptic plane, and separating the sky into two GLAT ranges, the situation is very difficult to interpret. To understand if the same pattern persists across the sky rather than presenting only for the all-sky average, we repeat the correlation analysis for GLAT bins. For each degree of galactic latitude, we cross correlate that Planck modified blackbody fitting results vs. the AME and the AKARI 9 micron intensity. (This comes with the caveat that the galactic plane is much more heavily sampled than the galactic poles.) Figure 3.1 shows the results.

#### 3.2. Analysis of Planck Collaboration AME Candidate Regions

Previously, Planck Collaboration et al. (2014c) (hereafter, PCXV) had identified and analyzed a list of regions where the AME appeared to stand out, relative to estimates of known microwave foregrounds. The full set includes 98 regions. While the majority of these regions showed only low significance AME, or a high potential contribution from free-free emission, 27 of showed highly significant AME. We re-examined the full set of 98 regions, employing data from 19 photometric bands, from the AKARI, Planck, IRAS, and WISE data sets. The major goals are 1) To see how the AME to IR comparison looks with the AKARI data, and 2) To apply a dust SED fitting analysis to these regions. While tackling these goals, we attempted to keep our analysis comparable as possible to the PCXV analysis by following their circular aperture photometry scheme. The process can be summarized as follows:

- 1) For each region, the total flux within a 1 degree radius circular aperture is summed.
- 2) A background annulus, with inner radius  $80'$  and outer radius  $100'$ , is placed around the source

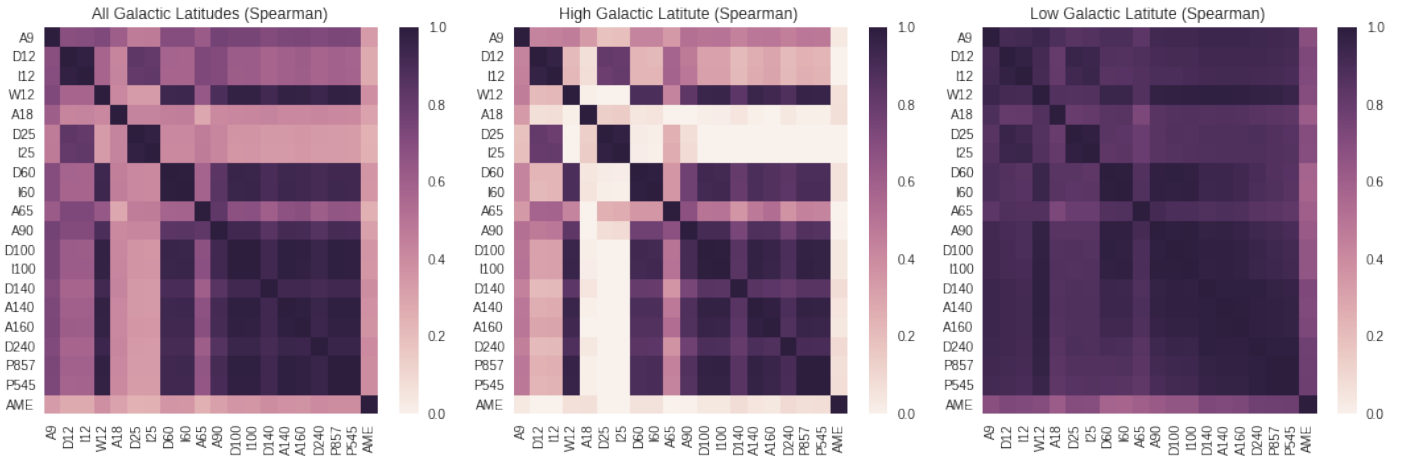


Fig. 3.— A colorized visualization of the ALL-SKY cross-correlation matrix for the 19 infrared bands sampled and the AME map. These results are based on the full sky (but omitting pixels within 10 degrees of the ecliptic plane) cross correlation of each band vs. every other band and the AME map. Plots on the top row are based on the Spearman rank correlation test. Those on the bottom are based on the Pearson correlation coefficients.

aperture. The median value of pixels inside the annulus is taken, and then scaled up to solid angle of the central source aperture. This is used as background level, to be subtracted from the source flux.

3) The noise level is estimated from the standard deviation of the background annulus pixels (estimating the noise level of large regions such as these is not a straightforward task.) We should note that for a few regions, the photometry done here using the PR2 map, and the photometry done on the same regions in PCXV, show discrepancies in the total flux measured (see Figure 3.2). These discrepancies do not alter our conclusions.

Once photometry results were gathered for all of the 98 regions, we then performed a full dust SED fitting,

The SED of the different fields were fit using the Galliano et al. (2011) dust model. We used the amorphous carbon and silicate dust mixture. Indeed, this dust mixture is more emissive than the standard silicate-graphite (Draine & Li 2007), by a factor of 2-3. As was shown by Herschel, in the LMC (Galliano et al. 2011), and by Planck, in the Milky Way (Planck Collaboration et al. 2016c), this increase of emissivity is necessary to have a proper fit of the sub-mm emission. We assume that the radiation field heating this dust mixture

is the Galactic ISRF (Mathis et al. 1983), scaled by a factor  $U$ . We also assume, following Dale et al. (2001), that the dust is exposed to a distribution of starlight intensity, distributed as:

$$dM_{dust} \propto U^{-\alpha} dU \quad (1)$$

between  $U_{min}$  and  $U_{max}$ , where  $U_{min}$ ,  $U_{max}$  and  $\alpha$  are free parameters. An old stellar population template (PEGASE; (Fioc & Rocca-Volmerange 1997)) is added to this SED in order to model the near-IR emission. The emission of this dust model is demonstrated in Fig. 3.2. We perform, for the moment, a simple least-squares analysis. The results of the SED fitting vs. the AME are shown in Figure 3.2. For the vast majority of the samples, the fits are reasonable, with the  $\chi^2$  distribution (see Fig. 3.2) appearing as we expect.

Two comparisons are shown - AME vs. PAH mass and AME vs. total dust mass, for two different AME data sets. The AME (PR2) data indicates the results of this work (our own photometry on the publicly available Planck 'COMMANDER' algorithm based AME map.) The AME (PCXV) plots, on the bottom, indicate that the AME flux values are those quoted from the PCXV analysis (wherein component separation, of AME from

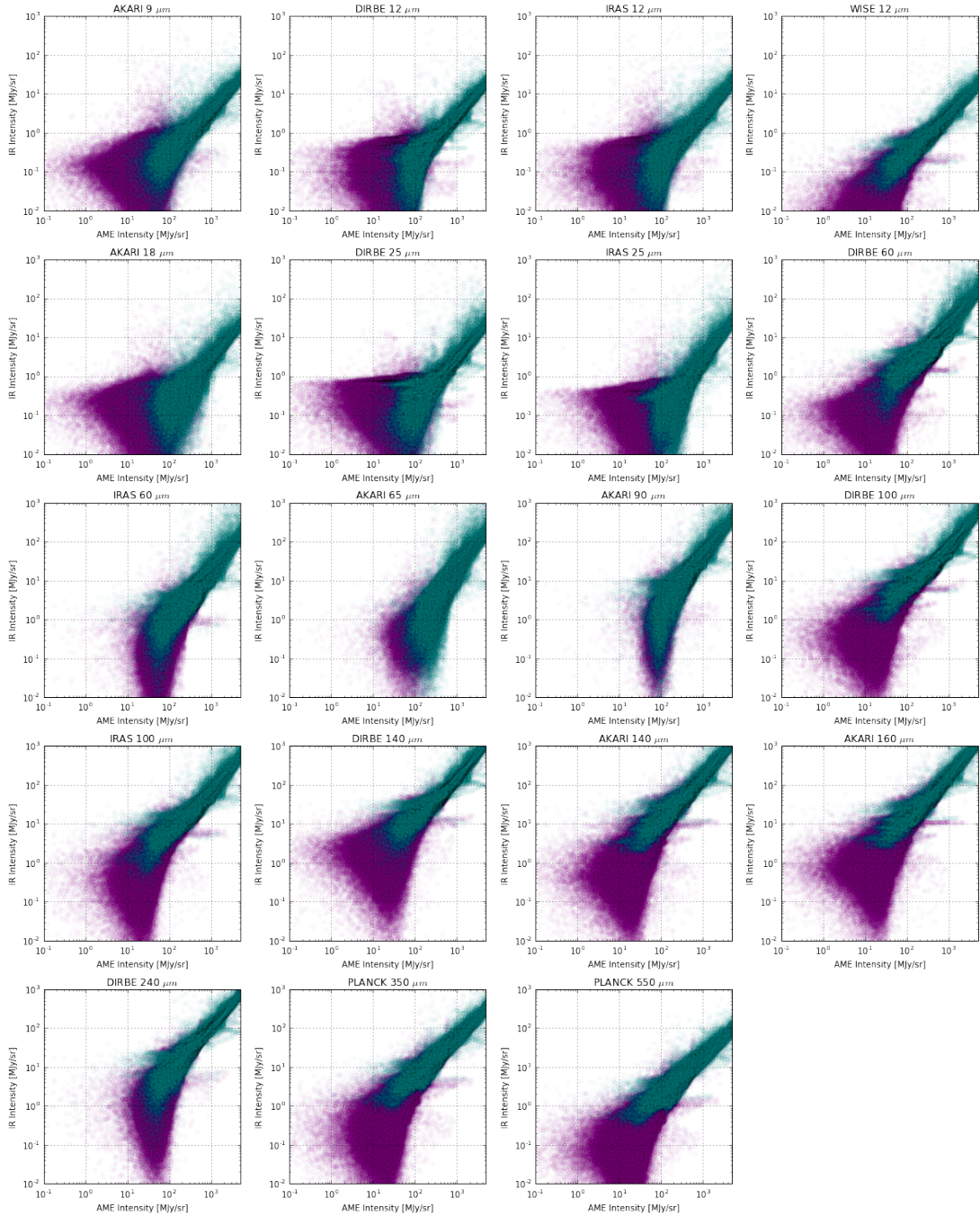


Fig. 4.— ALL-SKY plots of each of the 19 infrared bands' photometry results against those of the AME map. Similar to plots from the previous section, however these are produced on an all-sky basis. Cyan points represent pixels within 5 degrees of the galactic plane. Magenta points are pixels over 5 degrees from the galactic plane. Pixels within 5 degrees of the ecliptic plane are not plotted. Due to the large number of pixels plotted, a low alpha value is used (0.02). This helps to visualize the bulk of the pixels, but also means that portions of the plot with low point-density may seem blank on the page. Figure 3.1 shows the cross-correlation test results.

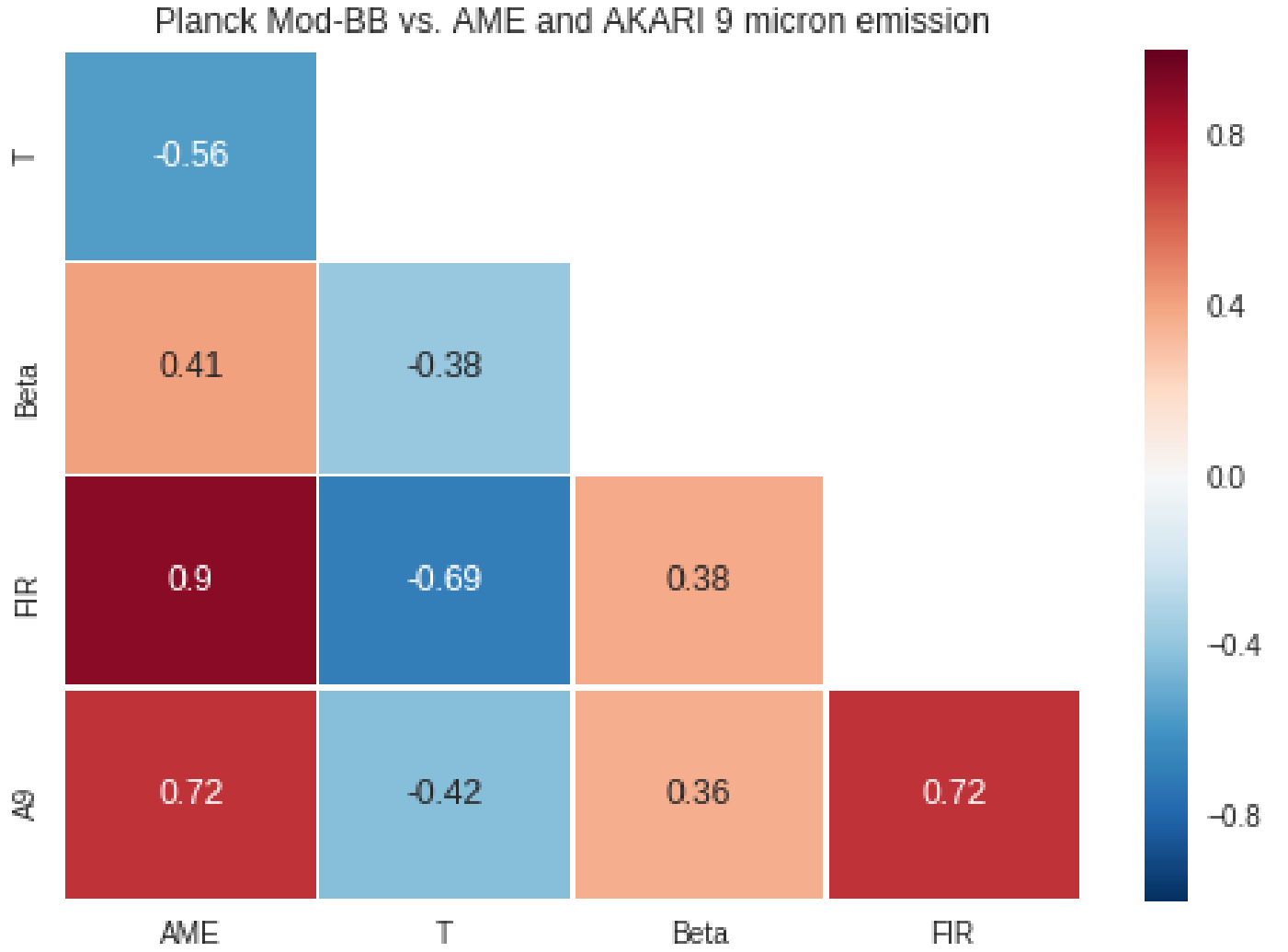


Fig. 5.— A cross-correlation test (Spearman) of AME vs. dust radiance (R), temperature (T), emissivity index (Beta), and the AKARI 9 micron brightness (A9), of the whole sky. Thermal dust parameters are provided in the Planck Coll. PR2 data. This provides a simplified picture of the AME vs. IR dust emission relationship. We can see that the results are consistent with the cross-correlation of AME vs. the 19 photometric intensities in Figure 3.1. This plot gives the results using the whole sky. Figure 3.1 shows correlation results broken down into 1-degree GLAT bins.

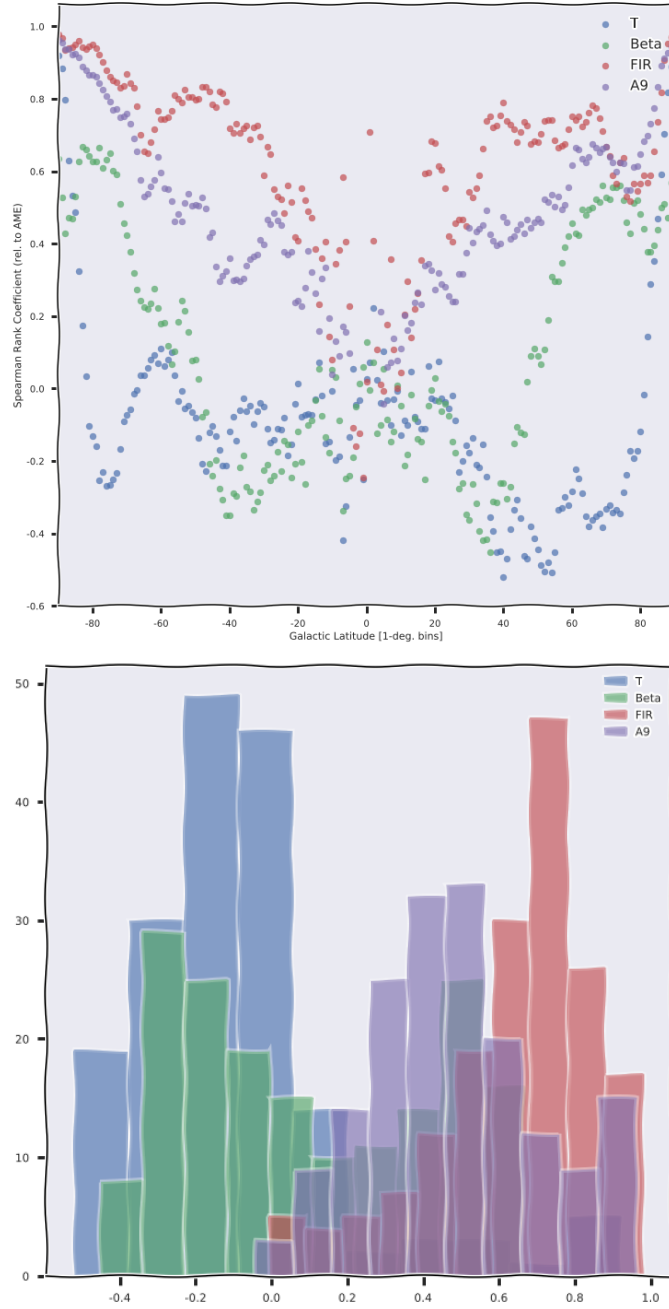


Fig. 6.— A cross-correlation tests (Spearman) of AME vs. dust radiance ( $R$ ), temperature ( $T$ ), emissivity index ( $\text{Beta}$ ), and the AKARI 9 micron brightness ( $A9$ ), by GLAT. The order of strongest to weakest correlation basically remains constant from pole to pole. (Except near the galactic plane, and around GLAT 40

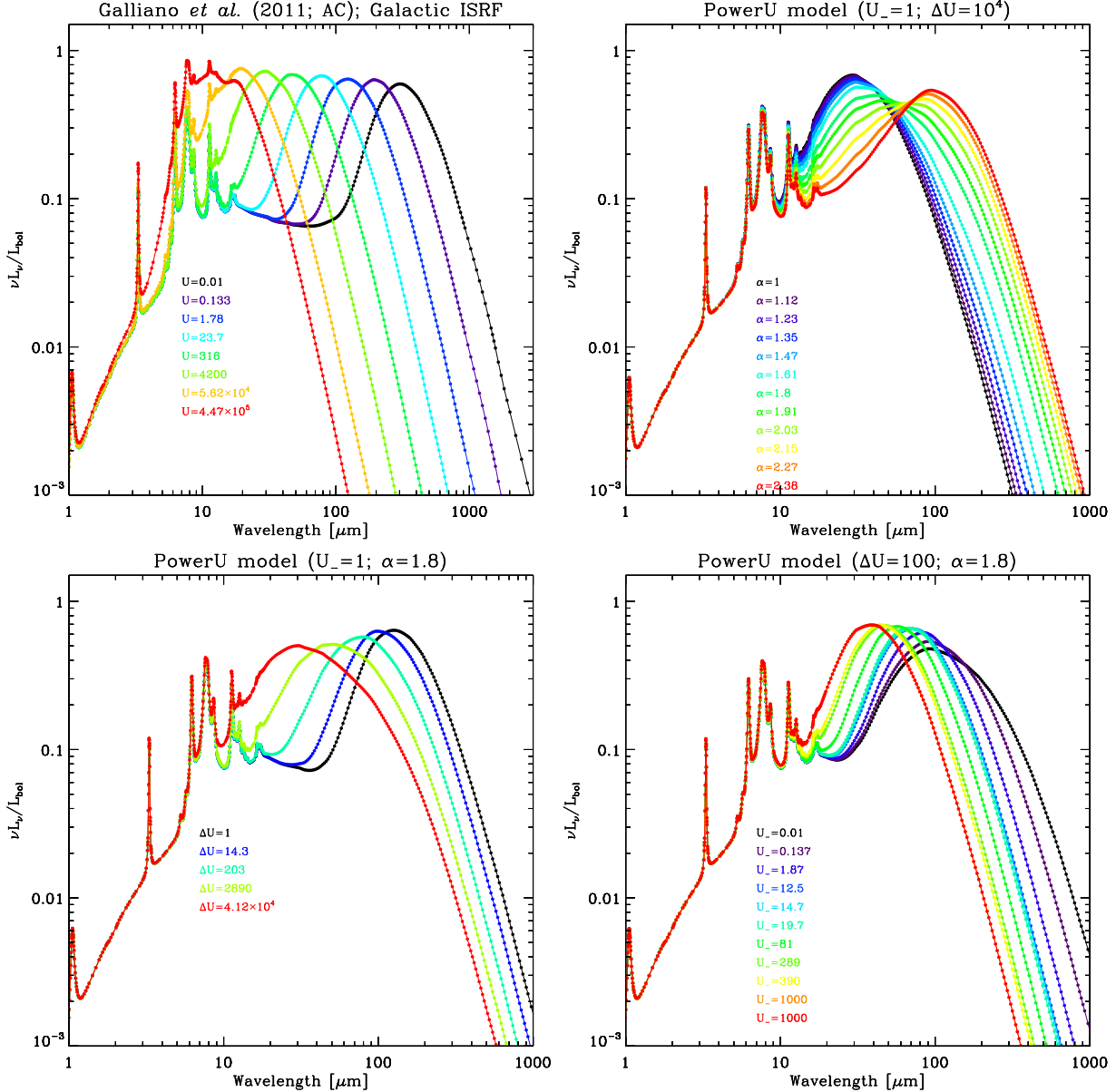


Fig. 7.— Dust templates of Galliano *et al.* (2011). The upper-left panel shows the variation of a uniformly illuminated mixture, as a function  $U$ . The other three panels show the variations of the emission of a dust mixture exposed to a distribution of starlight intensity, varying each parameter of Eq. 1.

known foregrounds, was done region-by-region.) Furthermore, the regions themselves are categorized as high (red circles) or low (blue circles) significance AME. Simply based on Figure 3.2, it is difficult to discern a difference on the correlation strengths. To statistically evaluate the situation, we employ the Bootstrap re-sampling approach, first introduced by Efron (1979). This involves creating 100,000 random re-sampled sets of the data. We use the "with replacement" approach, meaning that a data point may be selected multiple times in a single re-sampling iteration. However the size of the re-sampled set is the same as the input set size. For each random set we run a correlation test, resulting in a distribution of correlation coefficients. The results of the Bootstrap analysis are given in Figure 3.2. The distributions of correlation coefficients for AME vs. PAH mass, and AME vs. total dust mass., appear to be distinct. Mean correlation coefficients are separated by  $0.1+/-0.05-0.07$ .

### 3.3. Analysis of the $\lambda$ Orionis Region

Having looked at the AME vs. dust emission story on a very coarse scale, we now introduce our analysis of a particular region. The  $\lambda$  Orionis molecular ring, shown in Figure 3.3 as it appears in 1-degree smoothed AKARI 9  $\mu\text{m}$  data, indicates excess microwave emission attributed to AME (Planck Collaboration et al. 2016b). At approx. 10 degrees wide, we can see the outline of the structure even in the low (1 degree FWHM) resolution Planck-COMMANDER AME map. This is one of the only structures on the sky with a relatively well-distinguished shape at such low resolution. In order to shift towards an investigation of individual AME-prominent regions, we have carried out an initial comparison of the AME of this region with its mid to far-IR dust emission.

Figure 3.3 shows how the region looks, for 12 different photometric bands, from the mid to far IR. The contours show the region's structure as given by the Planck PR2 AME map. Figure 3.3 shows simple IR to AME cross correlation plots, for all pixels within the 10 by 10 degree  $\lambda$  Orionis region. Our findings for lambda  $\lambda$  Orionis indicate an AME-PAH correlation, but we are unable to argue for a causal link.

## 4. Discussion

As noted in Section 1, previous studies found that the AME generally correlates at dust-related IR wavelengths (Ysard et al. 2010; Planck Collaboration et al. 2014c; Hensley et al. 2016). We see the same overall pattern in the present study, for each of the three scales examined: the all-sky pixel-based analysis, the re-examination of Planck AME Candidate regions, and the inspection of the  $\lambda$  Orionis region. In the case of the AME candidate regions, do we find evidence of a statistically stronger relationship between AME and total dust mass than AME vs. PAH mass, for the full set of 98 regions. We were able to confirm that the correlation coefficients are statistically distinct, via bootstrap re-sampling (with replacement.) However the difference is marginal. Moreover the full set of 98 regions includes many regions that are either near the galactic plane, or do not have a strong S/N for the AME component separation. A similar result is found when we compare AME to the total dust luminosity and PAH luminosity.

The closeness of the correlation coefficients found here is consistent with the results of the IRAS vs. AME correlation test result from Planck Collaboration et al. (2014c). They found that correlation coefficient among the 4 IRAS bands (12, 25, 60, and 100 microns) differ from one another only by about 5%, across the whole set of 98 regions. The trend of AKARI MIR and FIR data vs. the AME does not disagree with their IRAS comparison. This work adds that bands longer than IRAS 100 micron also correlate strongly with AME, especially the two Planck/HFI bands used.

In the case of  $\lambda$  Orionis, we do not apply a dust SED fitting, but we did find that the AKARI 9 micron emission and the longest wavelength Planck 545 GHz emission had the strongest Spearman rank correlation coefficients (0.80 and 0.81.) The literature does not yet contain a comparable analysis of AME in  $\lambda$  Orionis, however if we consider the 9 micron band to be a tracer of PAH emission, and Planck 545 Ghz band to be a tracer of thermal dust emission, the result is in-line with what we have seen in Ysard et al. (2010) and Hensley et al. (2016). In those works, the two relationships (MIR vs. AME and FIR vs. AME) are very close (although these two papers are odds as to which relationship is stronger, and in their final inter-

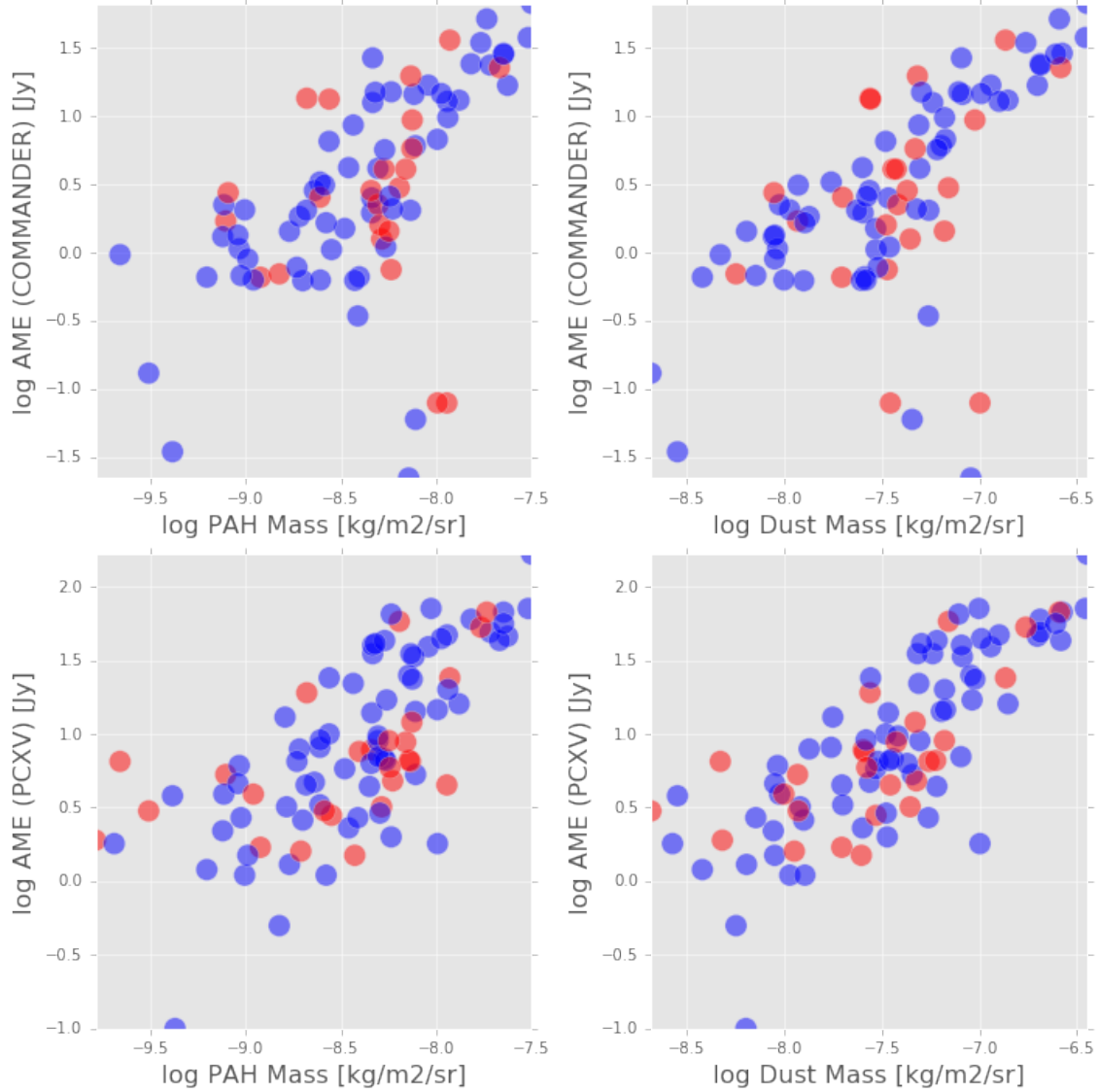


Fig. 8.— Results of circular aperture photometry and dust SED fitting for 98 regions listed in PCXV. Red dots indicated regions with significant AME. Blue dots indicated regions with low/zero significance AME.

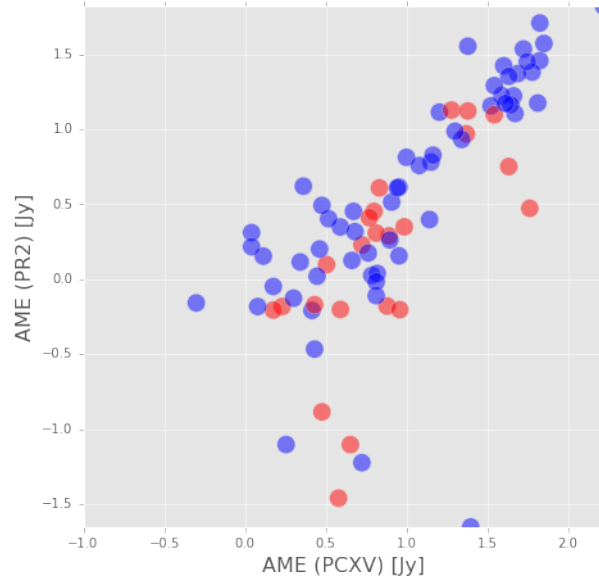


Fig. 9.— Left: Cross-comparison of the PCXV photometry results and the results of this work, based on the Planck Collaboration PR2 AME map.

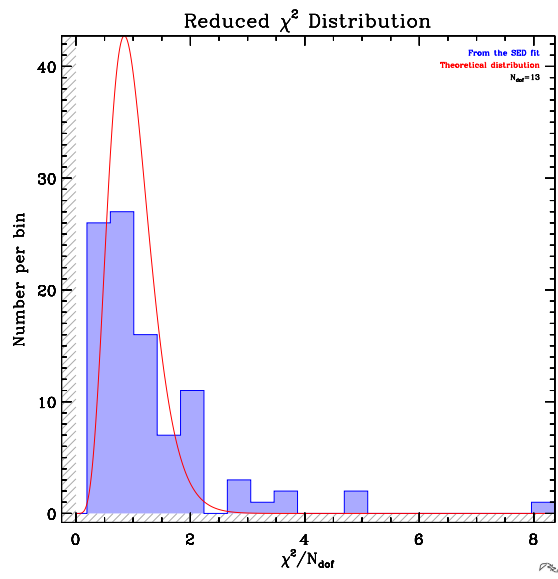


Fig. 10.— Histogram showing the  $\chi^2$  distribution of the dust SED fitting, to the AME region apertures.

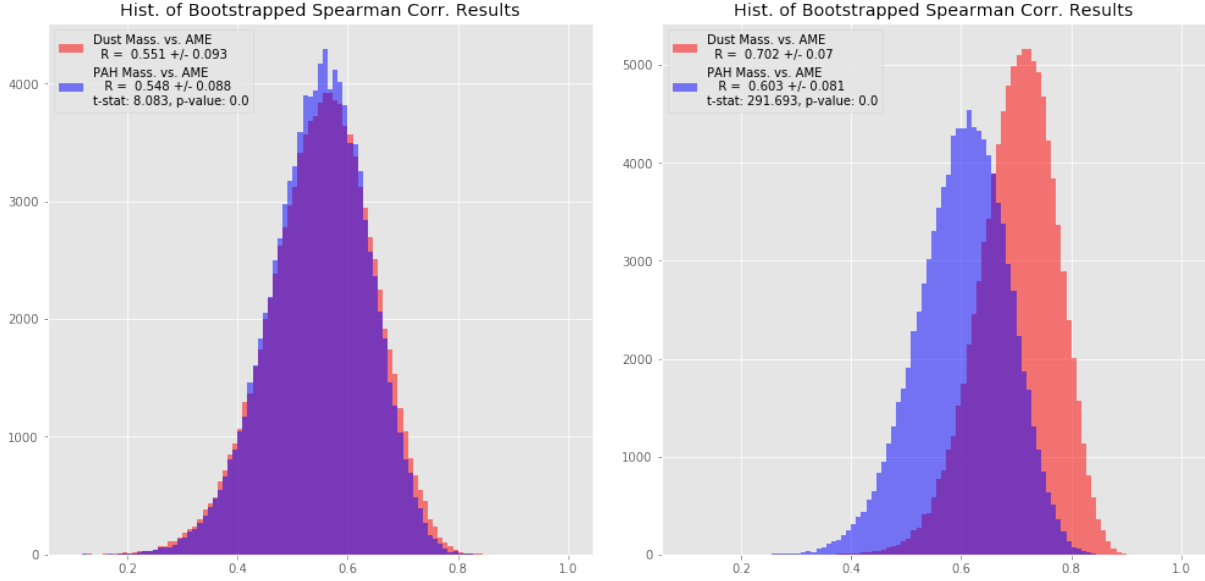


Fig. 11.— Top Left: Histogram showing the distribution of Pearson correlation coefficient results (R), based on 100,000 Bootstrapped sub-samples for each of the two comparisons (AME vs. total dust mass and AME vs. PAH mass.), based on PCXV AME flux values of the full set of 98 candidate regions. Top right: The same comparison, but using flux values obtained by directly performing circular aperture photometry on the Planck PR2 COMMANDER AME component map. Bottom left: PCXV bootstrap analysis using Spearman rank test. Bottom right: Spearman rank test for PR2 results. R values quoted for each comparison are that R-distribution's mean, and the error bars are the standard deviation.

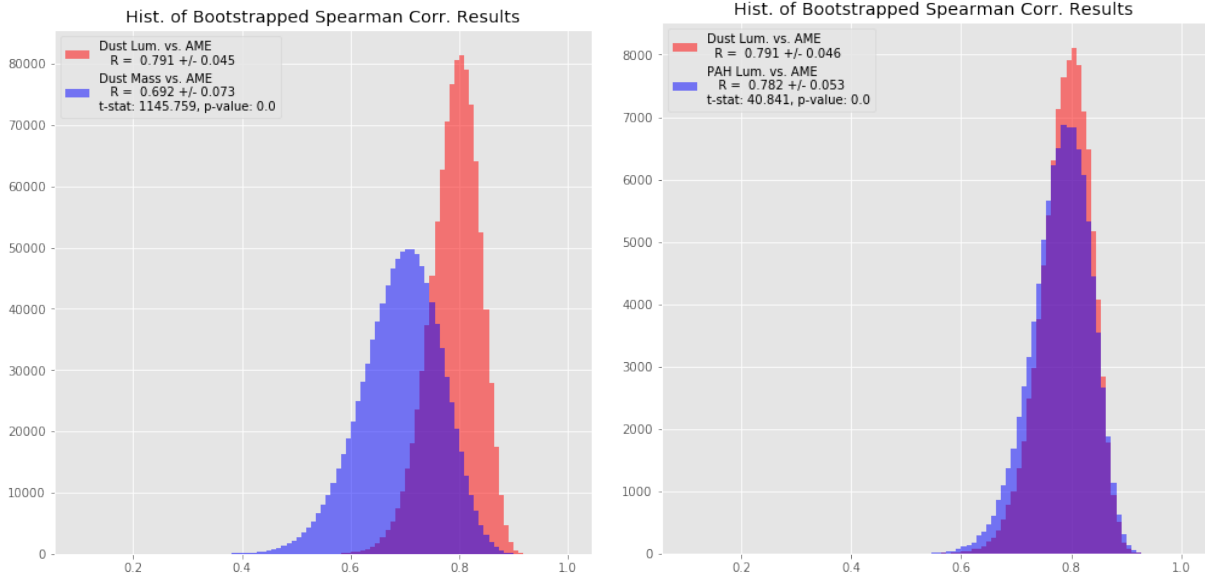


Fig. 12.— The plots above use the same comparison method as in Figure 3.2. However the dust fitting parameters being compared are

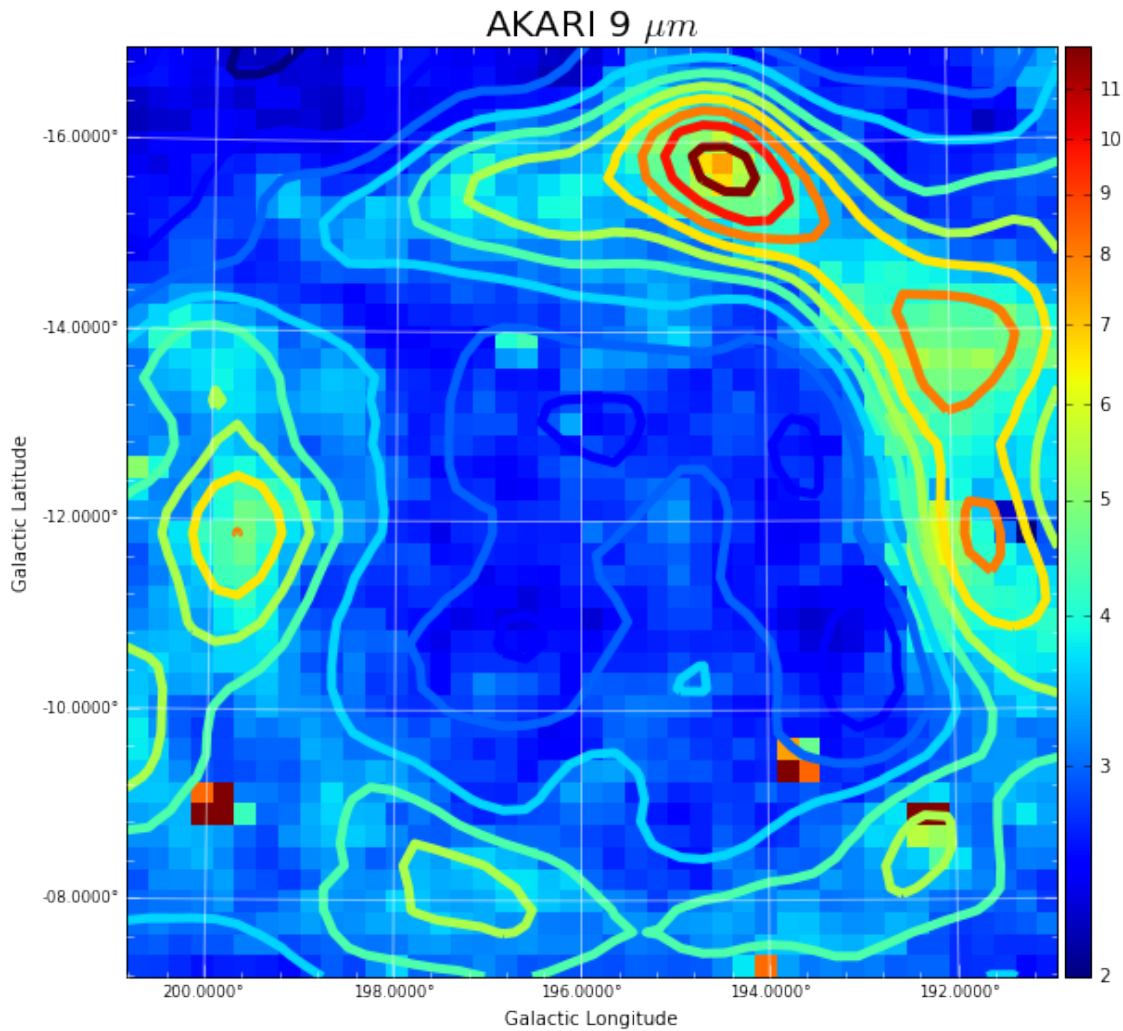


Fig. 13.—  $\lambda$  Orionis as it appears in the AKARI 9  $\mu\text{m}$  data. Contours indicate the AME, as given by the Planck PR2 AME map. The image is smoothed to a 1-degree PSF (much larger than the original 10 arcsec map. The  $\lambda$  Orionis star itself is approximately located at the center of the image. The dust wave structure, described by \*citation needed\*, is apparent, and seems to coincide with a local maxima in the PR2 AME contours. The units are MJ/sr. )

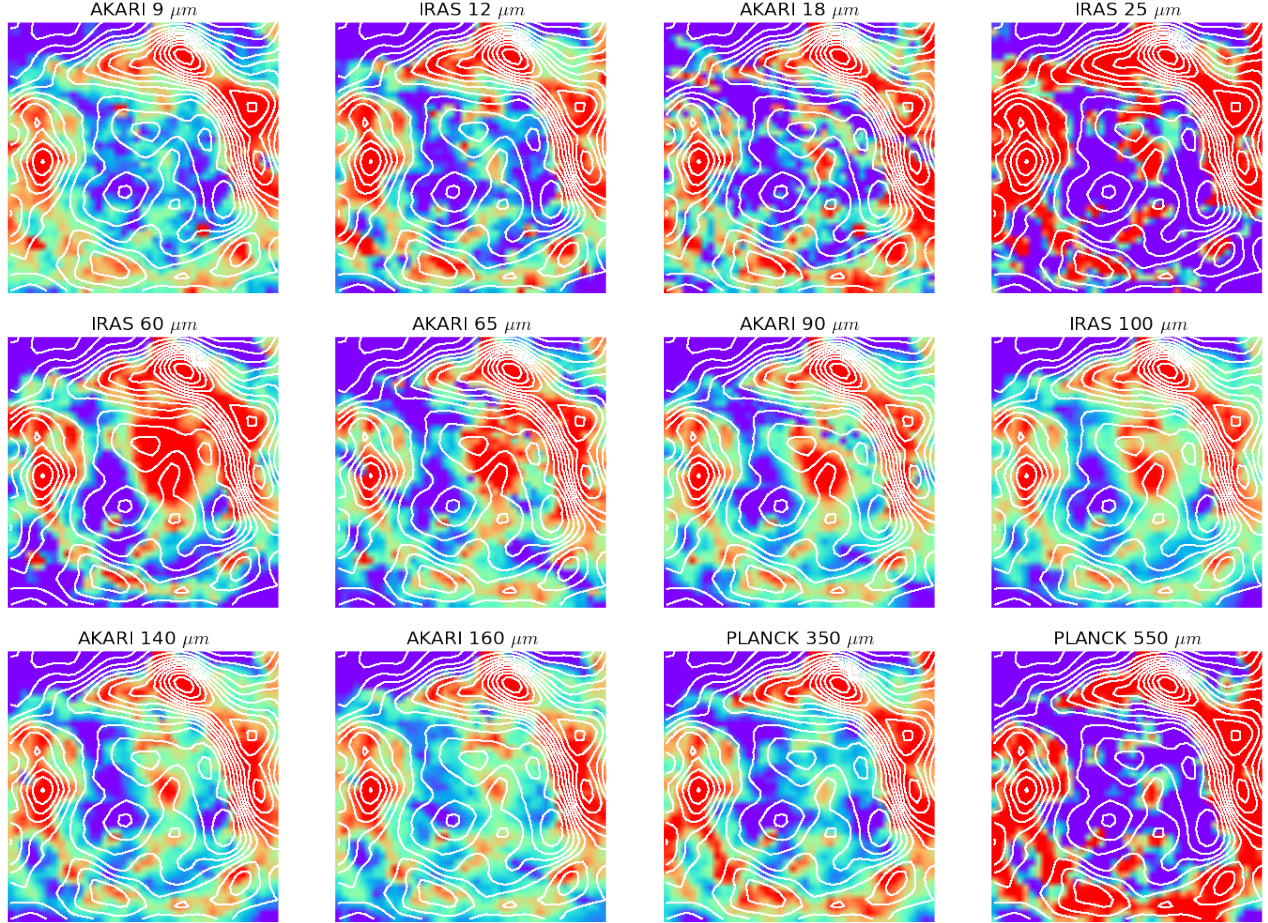


Fig. 14.— A grid of thumbnails showing the  $\lambda$  Orionis region's structure, at 12 wavelengths, along with AME contours (shown in white. Spatial correlation seems to be the best at the shortest and longest wavelengths (AKARI/IRC 9  $\mu m$  and Planck/HFI 550 micron) .

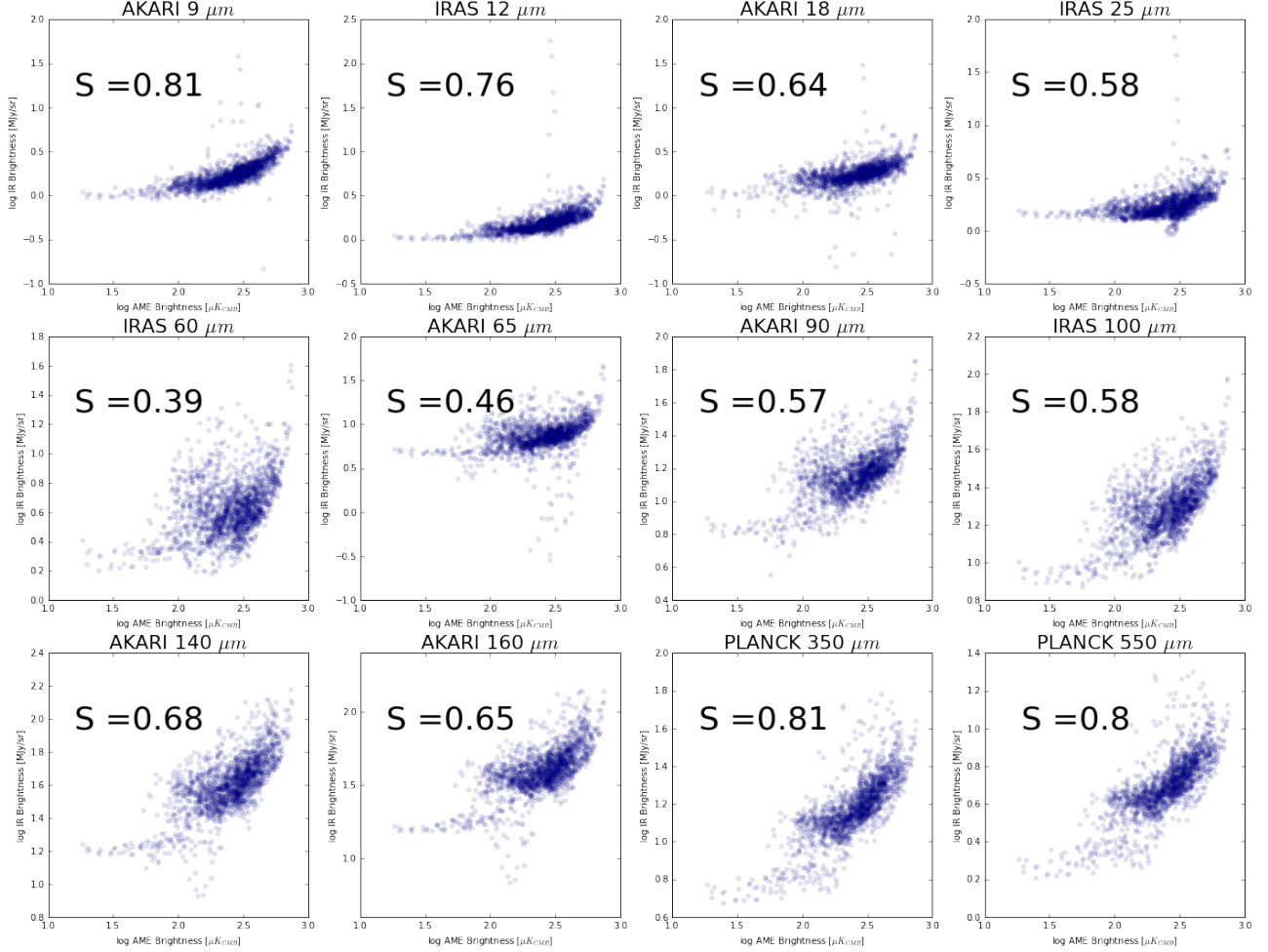


Fig. 15.— Pixel cross-correlation for all pixels in the  $\lambda$  Orionis cut-out region.  $S$  indicates the Spearman rank correlation coefficient for each plot.

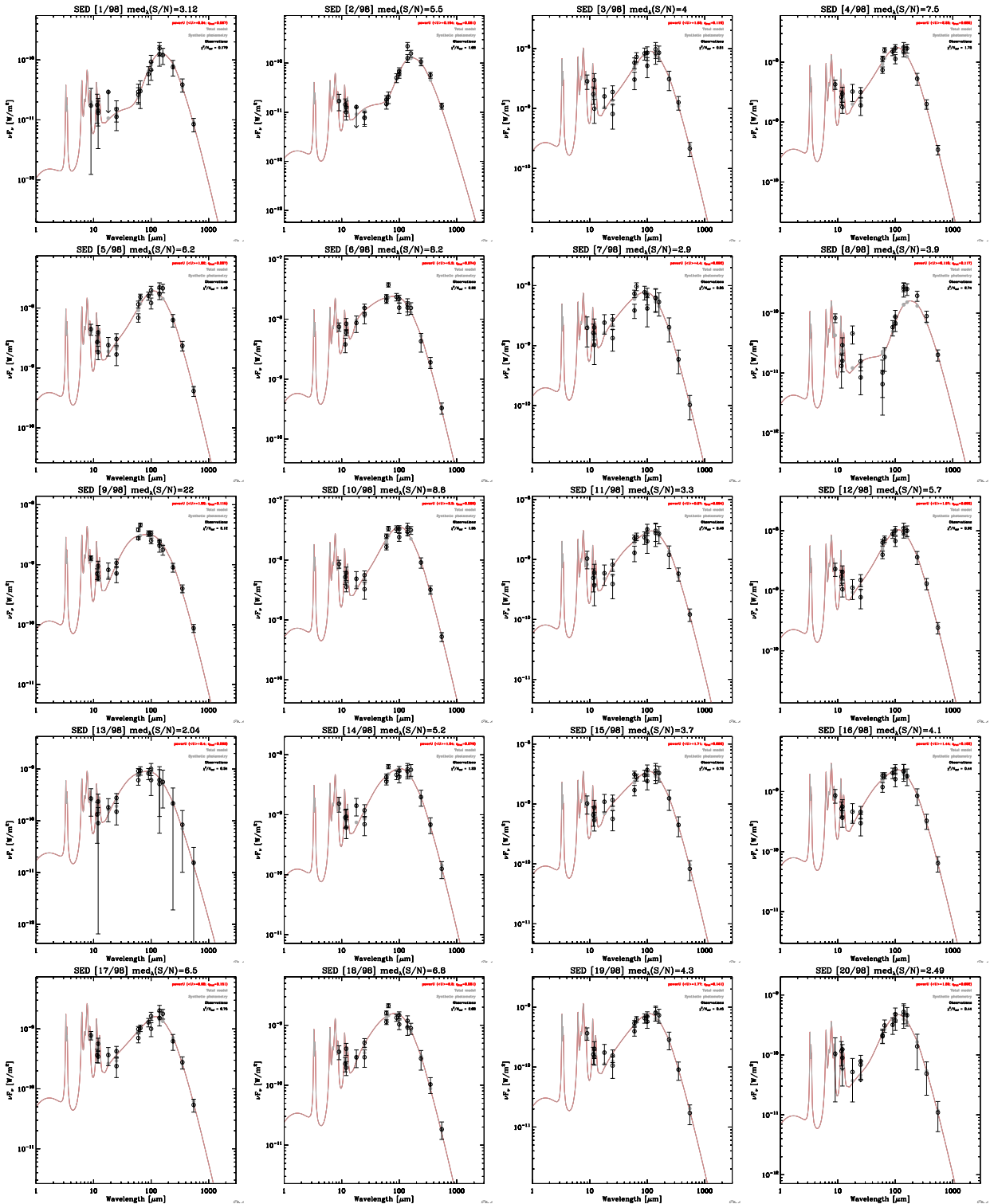
pretation.) In the future, we will apply the same dust SED fitting analysis, and bootstrap verification as was applied to the AME candidate regions described above. We will also attempt our own fitting of the AME component, based on low frequency data (rather than using the "COMMANDER" AME map.)

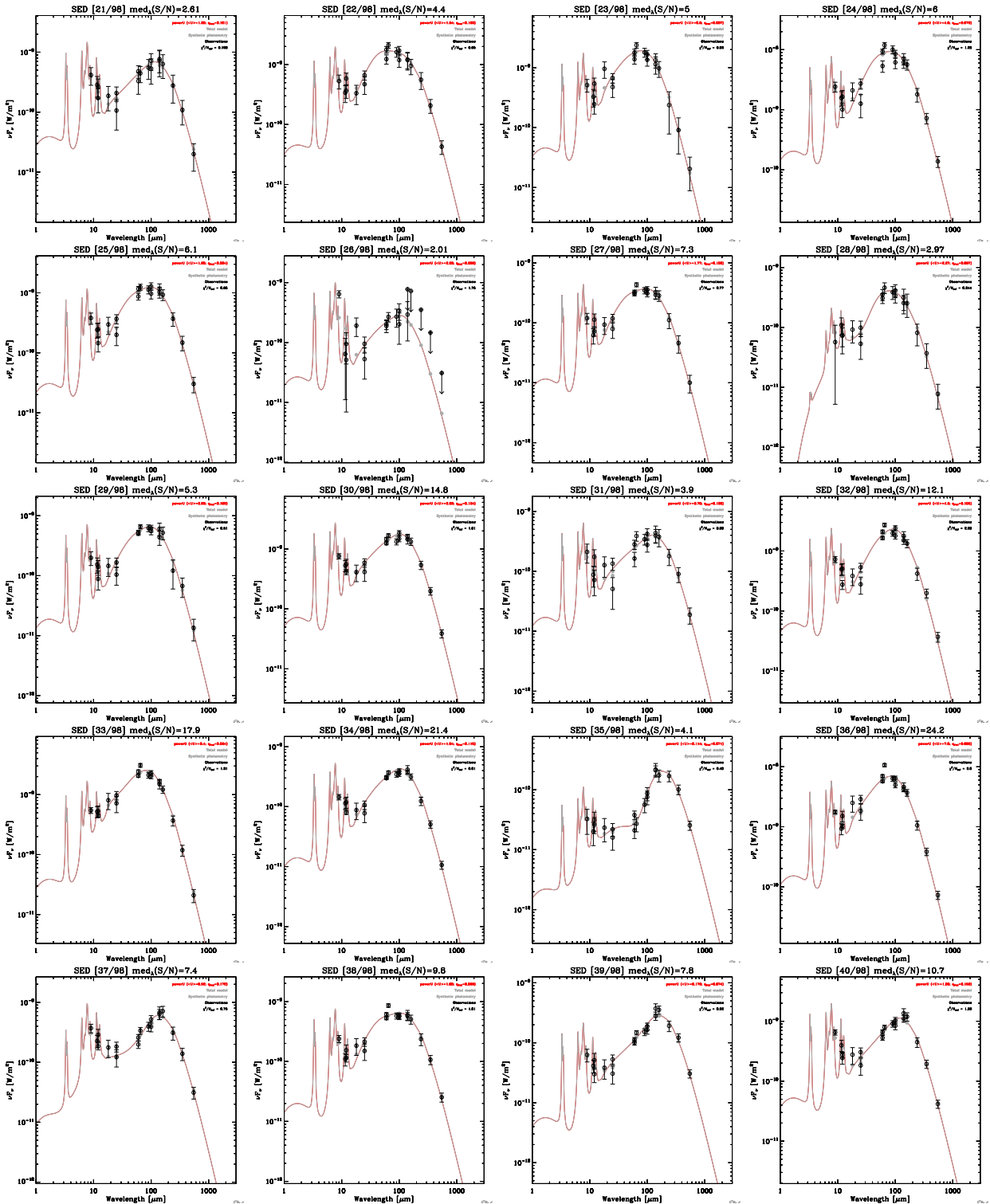
In our all-sky, pixel-by-pixel comparison, we find that all of the 19 wavelengths sampled show a first-order correlation with the AME. This is again consistent with the previous investigations of the AME cited above, wherein the only differences found are minor. Without applying further dust SED fitting, this analysis seems to concur with Hensley et al. (2016) in that the FIR bands (in their work, they used the dust radiance) show the tightest correlation. However, the difference in correlation from the MIR to FIR becomes very small when focusing only on galactic latitudes within 5 degrees of the plane. In Hensley et al. (2016), the galactic plane is masked, whereas we mask only the pixels which have missing data from any of the 19 maps, as well as pixels within 10 degrees of the ecliptic plane (due to residual zodiacal light emission in the MIR maps.)

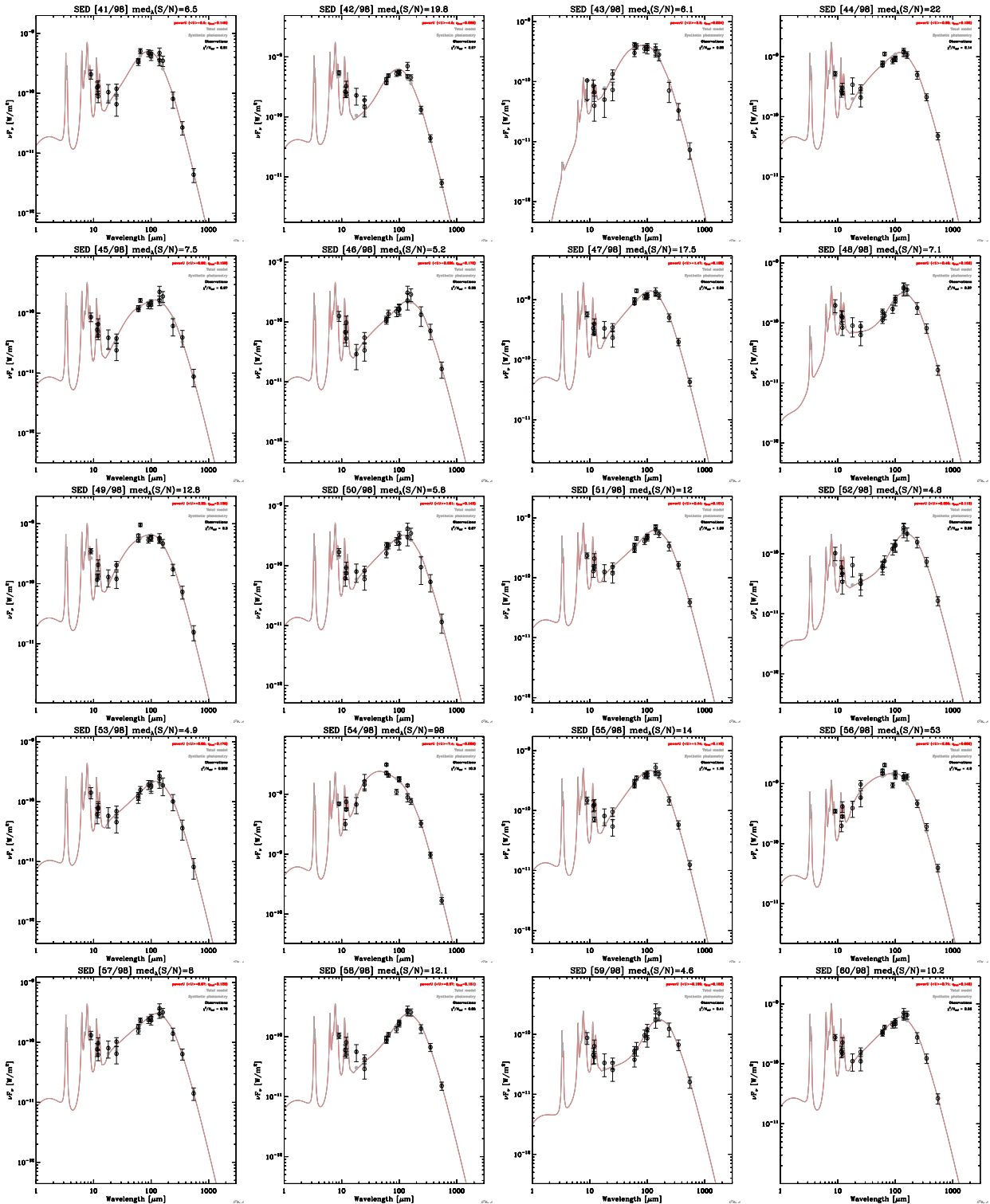
From these results, we cannot confirm or rule out a spinning-PAH hypothesis on an all-sky, 1-degree scale. However, in  $\lambda$  Orionis, the results may be consistent with a scenario in which PAH mass, cold dust, and the AME are all tightly correlated. Weaker correlation from 25 to 70 microns may indicate that AME is weaker in regions of warmer dust and stronger radiation fields. Further analysis is needed to investigate if the AME seen in this region really comes from PAHs or other small spinning grains, and/or another source entirely. Future work should investigate whether or not PAHs are being destroyed in the region of  $\lambda$  Orionis where AME is weaker.

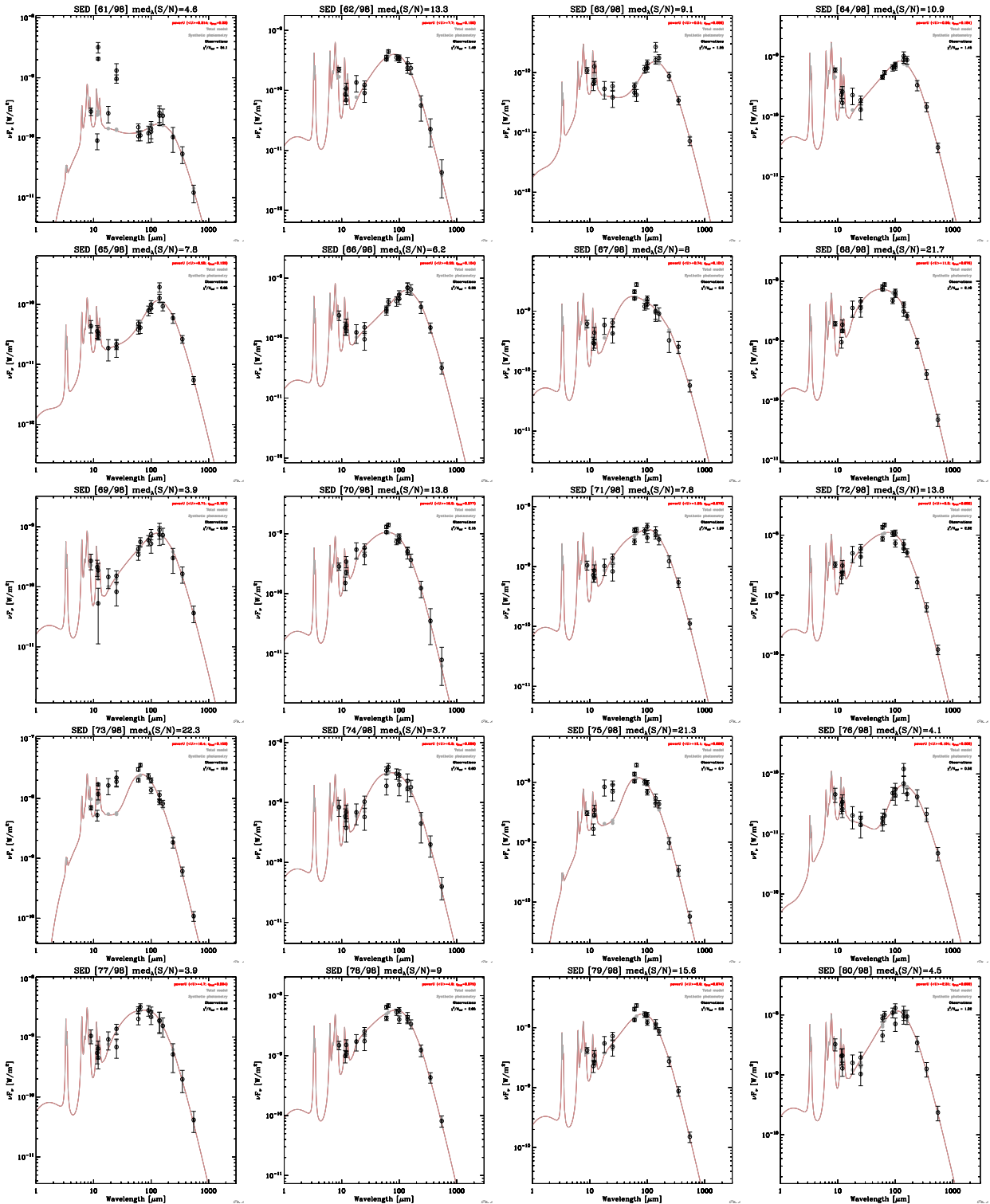
We look forward to continued environment-resolved comparisons to investigate the potential AME-PAH relationship in a region by region manner. We will explore  $\lambda$  Orionis in more detail, in a later paper. We will also employ higher resolution AME all-sky data as it becomes available.

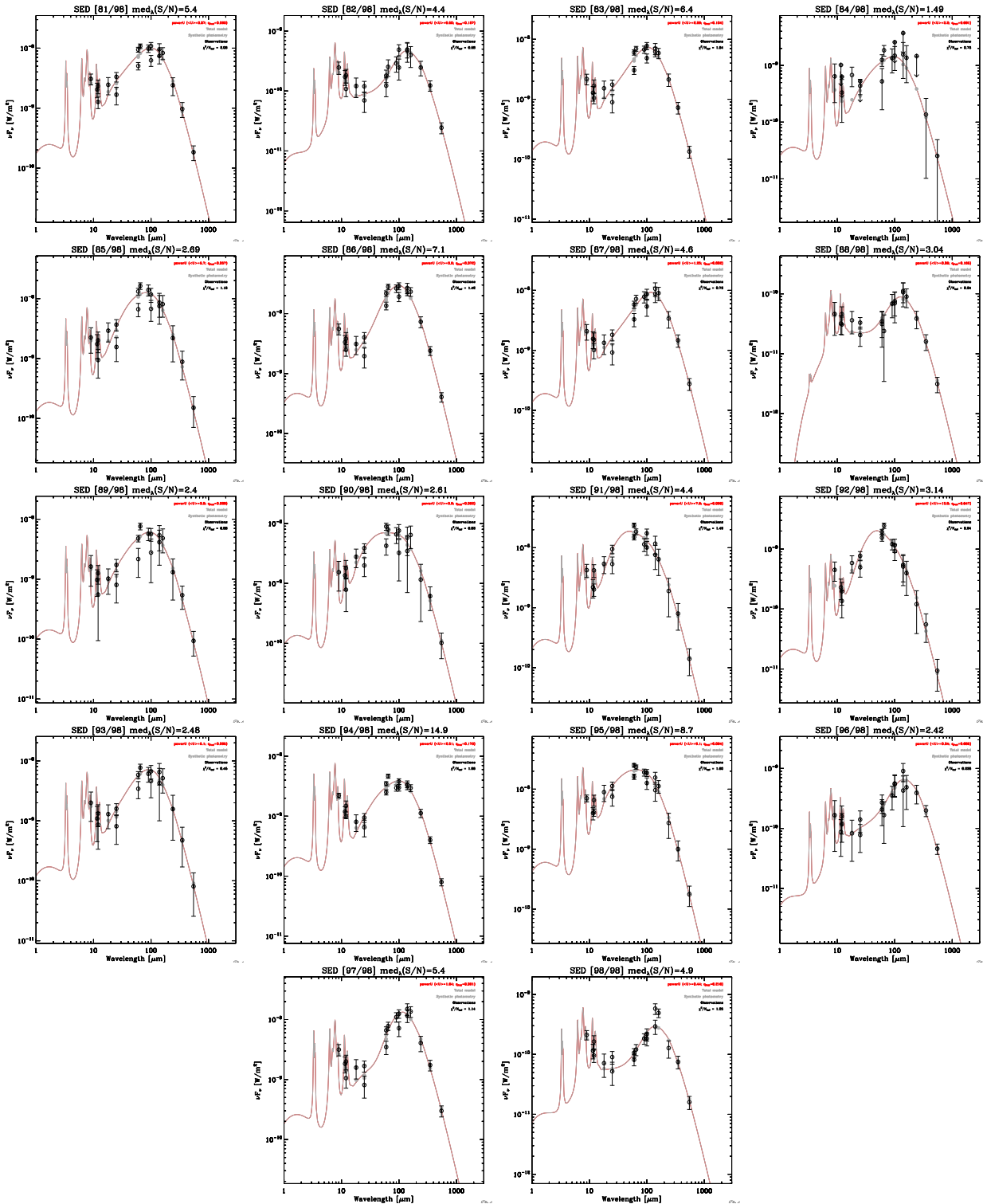
## A. Appendix: SEDs











## REFERENCES

- Ali-Haimoud, Y. 2010, SpDust/SpDust.2: Code to Calculate Spinning Dust Spectra, Astrophysics Source Code Library
- Ali-Haïmoud, Y. 2014, MNRAS, 437, 2728
- Ali-Haïmoud, Y., Hirata, C. M., & Dickinson, C. 2009, MNRAS, 395, 1055
- Andrews, H., Boersma, C., Werner, M. W., Livingston, J., Allamandola, L. J., & Tielens, A. G. G. M. 2015, ApJ, 807, 99
- Bonnarel, F., et al. 2000, A&AS, 143, 33
- Dale, D. A., Helou, G., Contursi, A., Silbermann, N. A., & Kolhatkar, S. 2001, ApJ, 549, 215
- de Oliveira-Costa, A., Kogut, A., Devlin, M. J., Netterfield, C. B., Page, L. A., & Wollack, E. J. 1997, ApJ, 482, L17
- Dickinson, C., Paladini, R., & Verstraete, L. 2013, Advances in Astronomy, 2013, 1
- Doi, Y., et al. 2015, PASJ, 67, 50
- Draine, B. T., & Hensley, B. 2013, ApJ, 765, 159
- Draine, B. T., & Lazarian, A. 1998, ApJ, 508, 157
- . 1999, ApJ, 512, 740
- Draine, B. T., & Li, A. 2001, ApJ, 551, 807
- . 2007, ApJ, 657, 810
- Efron, B. 1979, Ann. Statist., 7, 1
- Erickson, W. C. 1957, ApJ, 126, 480
- Ferrara, A., & Dettmar, R.-J. 1994, ApJ, 427, 155
- Fioc, M., & Rocca-Volmerange, B. 1997, A&A, 326, 950
- Galliano, F., et al. 2011, A&A, 536, A88
- Giard, M., Lamarre, J. M., Pajot, F., & Serra, G. 1994, A&A, 286
- Górski, K. M., Hivon, E., Banday, A. J., Wandelt, B. D., Hansen, F. K., Reinecke, M., & Bartelmann, M. 2005, ApJ, 622, 759
- Hensley, B. S., & Draine, B. T. 2017, ApJ, 836, 179
- Hensley, B. S., Draine, B. T., & Meisner, A. M. 2016, The Astrophysical Journal, 827, 45
- Hoang, T., Draine, B. T., & Lazarian, A. 2010, ApJ, 715, 1462
- Hoang, T., Vinh, N.-A., & Quynh Lan, N. 2016, ApJ, 824, 18
- Hoyle, F., & Wickramasinghe, N. C. 1970, Nature, 227, 473
- Ishihara, D., et al. 2010, A&A, 514, A1
- Jones, A. P. 2009, A&A, 506, 797
- Kawada, M., et al. 2007a, PASJ, 59, 389
- . 2007b, PASJ, 59, S389
- Kelsall, T., et al. 1998, ApJ, 508, 44
- Kogut, A., Banday, A. J., Bennett, C. L., Gorski, K. M., Hinshaw, G., & Reach, W. T. 1996, ApJ, 460, 1
- Kondo, T., et al. 2016, AJ, 151, 71
- Leitch, E. M. 1998, PhD thesis, CALIFORNIA INSTITUTE OF TECHNOLOGY
- Lovas, F. J., McMahon, R. J., Grabow, J.-U., Schnell, M., Mack, J., Scott, L. T., & Kuczkowski, R. L. 2005, Journal of the American Chemical Society, 127, 4345, pMID: 15783216
- Maddalena, R. J. 1986, PhD thesis, National Aeronautics and Space Administration. Goddard Inst. for Space Studies, New York, NY.
- Maddalena, R. J., & Morris, M. 1987, ApJ, 323, 179
- Mathis, J. S., Mezger, P. G., & Panagia, N. 1983, A&A, 128, 212
- Miville-Deschénes, M.-A., & Lagache, G. 2005, ApJS, 157, 302
- Murakami, H., et al. 2007, PASJ, 59, 369
- Neugebauer, G., et al. 1984, ApJ, 278, L1
- Onaka, T. 2000, Advances in Space Research, 25, 2167
- Onaka, T., Yamamura, I., Tanabe, T., Roellig, T. L., & Yuen, L. 1996, PASJ, 48, L59
- Onaka, T., et al. 2007, PASJ, 59, 401
- Planck Collaboration et al. 2014a, A&A, 571, A8
- . 2014b, A&A, 571, A12
- . 2014c, A&A, 565, A103
- . 2016a, A&A, 594, A10
- . 2016b, A&A, 594, A25
- . 2016c, A&A, 586, A132
- Takita, S., et al. 2015, PASJ, 67, 51
- Thorwirth, S., Theulé, P., Gottlieb, C. A., McCarthy, M. C., & Thaddeus, P. 2007, ApJ, 662, 1309
- Tibbs, C. T., et al. 2011, MNRAS, 418, 1889
- Ysard, N., Juvela, M., & Verstraete, L. 2011, A&A, 535, A89
- Ysard, N., Miville-Deschénes, M. A., & Verstraete, L. 2010, A&A, 509, L1
- Ysard, N., & Verstraete, L. 2010, A&A, 509, A12